Supporting Information

The *in-situ* structural evolution of Bi_2O_3 facilitates the electrocatalytic hydrogenation of oxalic acid to glycolic acid

Donghai Chen, [a] Haolin Cheng, [a] Yan Fu, [*a] and Jinli Zhang, [*ab]

[a] School of Chemical Engineering and Technology, Tianjin University, Tianjin 300350, China

[b] School of Chemistry and Chemical Engineering/State Key Laboratory Incubation Base for Green Processing of Chemical Engineering, Shihezi University, Shihezi 832003, China

[*] Corresponding authors.

E-mail: fuyan@tju.edu.cn; zhangjinli@tju.edu.cn.

Materials and methods

Chemicals and materials

The chemicals and materials utilized in this work included bismuth (III) nitrate pentahydrate ($Bi(NO_3)_3 \cdot 5H_2O$, 99.0%, Shanghai Mindray Biochemical Technology Co., Ltd), ethylene glycol ($C_2H_6O_2$, AR, Tianjin Kermel Chemical Reagent Co., Ltd), polyvinyl pyrrolidone (PVP-K30, AR, Tianjin Guangfu Fine Chemical Research Institute) and sulfuric acid (H_2SO_4, 95~98 wt%, Tianjin Jiangtian Chemical Technology Co., Ltd.). Oxalic acid ($C_2H_2O_4$, 98%), glyoxylic acid ($C_2H_2O_3$, 98%) and glycolic acid ($C_2H_4O_3$, 98%) were purchased from Tianjin Hiens Optus Technology Co., Ltd. Nafion 117 membrane (DuPont, USA) was obtained from Jingchong Electronic Technology Development Co., Ltd.

Characterizations

The microstructure and phase compositions of the as-prepared catalysts were characterized through field emission scanning electron microscopy (SEM) (Apreo S LoVac), JEM-F200 transmission microscopy (TEM), X-ray diffraction (XRD, SmartLab with Cu Kα radiation), X-ray photoelectron spectroscopy (XPS, Thermo Fisher Scientific K-Alpha+) and inductively coupled plasma optical emission spectrometry (ICP-OES, Agilent 5110). Electron paramagnetic resonance (EPR) spectra of the samples were collected on a Bruker EMX-plus ESR spectrometer. Products for the ECH of OX were determined by high performance liquid chromatography (HPLC, Agilent 1200) equipped with an Aminex HPX-87H column (300 × 7.8 mm) and an ultraviolet detector (UVD). Raman and *in-situ* Raman spectra were obtained from confocal Raman microscopy (Horiba LabRAM HR Evolution) with a laser of 633 nm and 1800 g/mm diffraction grating. Electrochemical *in situ* ATR-SEIRAS measurements were performed on the FT-IR spectrometer (iS50, Nicolet) with a modified accessory (VeeMax III, PIKE Technology) and MCT-A detector cooled with liquid nitrogen.

Electrochemical measurements

Electrochemical measurements were performed utilizing the CHI760E workstation in a three-electrode system. The as-prepared electrode, Ag/AgCl electrode, and Pt plate were used as the working, reference, and counter electrode, respectively. The geometric surface area for the working electrode is 1 cm^2 (1.0 cm × 1.0 cm). Each potential was calibrated to the reversible hydrogen electrode by the following equation:

$$E_{RHE} = E_{Ag/AgCl} + 0.197 + 0.059pH$$

Prior to conducting any tests, the working electrodes were pre-activated by cyclic voltammograms (CV) acquiring from 0.1 to −0.9 V vs RHE at a scan rate 100 mV s^{-1}. Linear scan voltammetry (LSV) curves occurred at a scan rate of 5 mV s^{-1} in 0.05 M H_2SO_4 with 100 mM OX added, complemented by 85% iR correction. The related Tafel slopes (b) were determined using the equation (E is the overpotential and j is the current density):

$$E = a + b\ log\ j$$

Electrochemical active surface area (ECSA) was derived from the CV curves by the double-layer capacitance (C_{dl}) method under non-Faradaic regions.[1] It was estimated in a potential scan range from 0.712 to 0.812 V vs RHE with the scan rates of 20, 40, 60, 80, and 100 mV·s^{-1} in 0.05 M H_2SO_4 with 100 mM OX added. Electrochemical impedance spectroscopy (EIS) was acquired at −0.5 V vs RHE within the frequency range from 10^5 to 10^{-2} Hz.

Density functional theory (DFT) calculations

Density Functional Theory (DFT) calculations were conducted using the Vienna Ab initio Simulation Package (VASP), employing the Projector Augmented-Wave (PAW) method.[2] The exchange-correlation energy and potential were described using the Perdew-Burke-Ernzerhof (PBE) functional within the generalized gradient approximation (GGA).[3] A plane-wave basis set with a cutoff energy of 500 eV was employed. The Brillouin zone was sampled using a 2×2×1 Monkhorst-Pack grid. To prevent spurious interactions between periodic images, a vacuum layer with a thickness of 15 Å was introduced along the Z direction.

For the Bi/Bi_2O_3 model, the simulation combined the Bi_2O_3 (222) surface with a Bi monolayer. In the Bi configuration, the atoms in the bottommost layer were fixed, while all other atoms were permitted to relax. In the Bi/Bi_2O_3 configuration, the bottom three layers were fixed, while the remaining atoms were fully relaxed. Structural optimizations were conducted until the convergence criteria for energy and force were met, specifically 10^{-5} eV and 0.02 eV/Å, respectively. To accurately compute the density of states, the hybrid Heyd-Scuseria-Ernzerhof (HSE06) functional was used, and the K-point grid was refined to 3×4×1.[4] The reaction pathways involved in the calculation of the catalytic hydrogenation of OX are as follows:

$$* + \mathrm{HOOCCOOH} \rightarrow \mathrm{HOOCCOOH}^* \qquad (1)$$

$$HOOCCOOH^* + H^+ + e^- \rightarrow HOOCCO^* + H_2O \qquad (2)$$

$$HOOCCO^* + H^+ + e^- \rightarrow HOOCCHO^* \qquad (3)$$

$$HOOCCHO^* + H^+ + e^- \rightarrow HOOCCHOH^* \qquad (4)$$

$$HOOCCHOH^* + H^+ + e^- \rightarrow HOOCCH_2OH^* \qquad (5)$$

$$HOOCCH_2OH^* \rightarrow HOOCCH_2OH + {}^* \qquad (6)$$

where * represents the group adsorbed on the surface. The Gibbs free energy (G) of the reaction intermediate is determined by the computational hydrogen electrode (CHE) model, and the G (T=298K) is expressed as: $G = E_{DFT} + E_0 - TS$,

where E_0 and S were considered as zero-point energy and entropy.

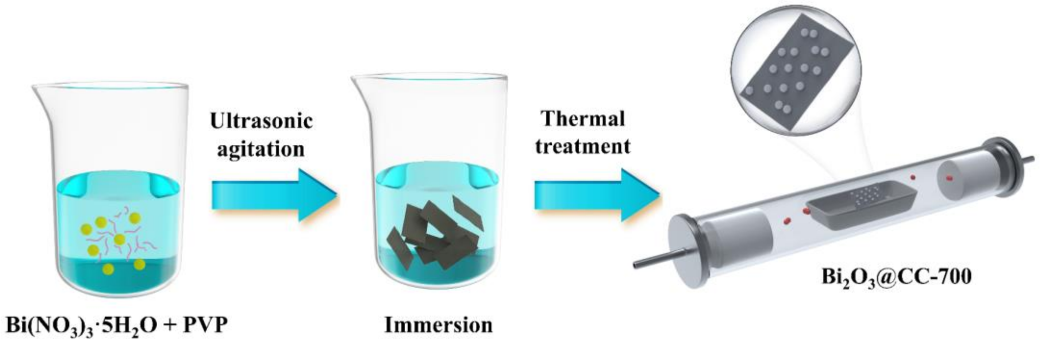

Fig. S1. Schematic illustration for the synthesis procedure of Bi_2O_3@CC-700.

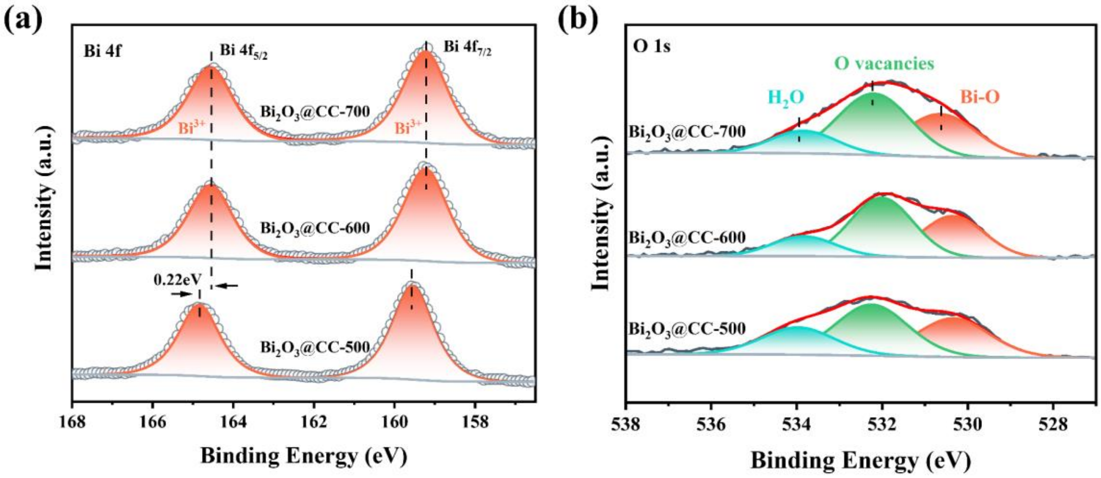

Fig. S2. High-resolution XPS spectra of Bi_2O_3@CC synthesized at various thermal treatment temperatures: (a) Bi 4f and (b) O 1s.

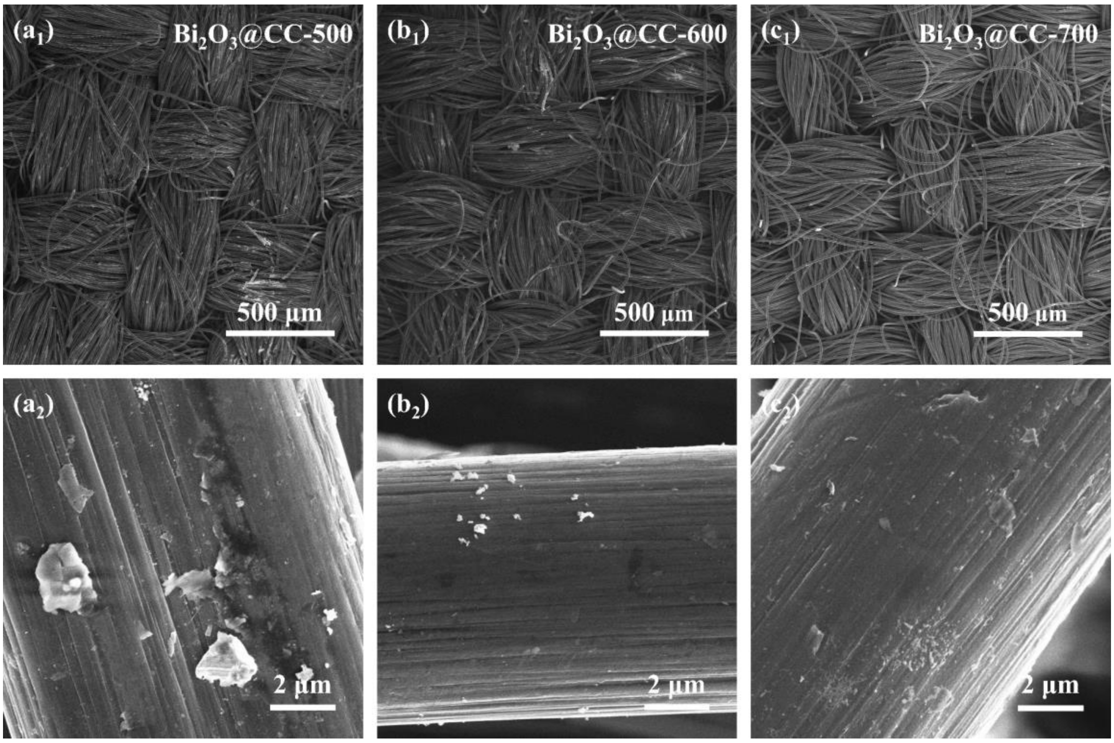

Fig. S3. The SEM images of Bi_2O_3@CC synthesized at various thermal treatment temperatures: (a) 500 ℃, (b) 600 ℃, and (c) 700 ℃.

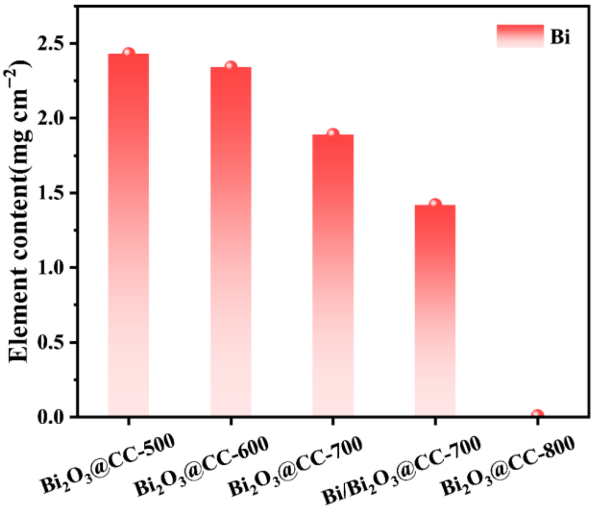

Fig. S4. The mass loadings of Bi for Bi_2O_3@CC-500, Bi_2O_3@CC-600, Bi_2O_3@CC-700, Bi/Bi_2O_3@CC-700 (ECH for 9 h) and Bi_2O_3@CC-800 respectively, determined by ICP-OES.

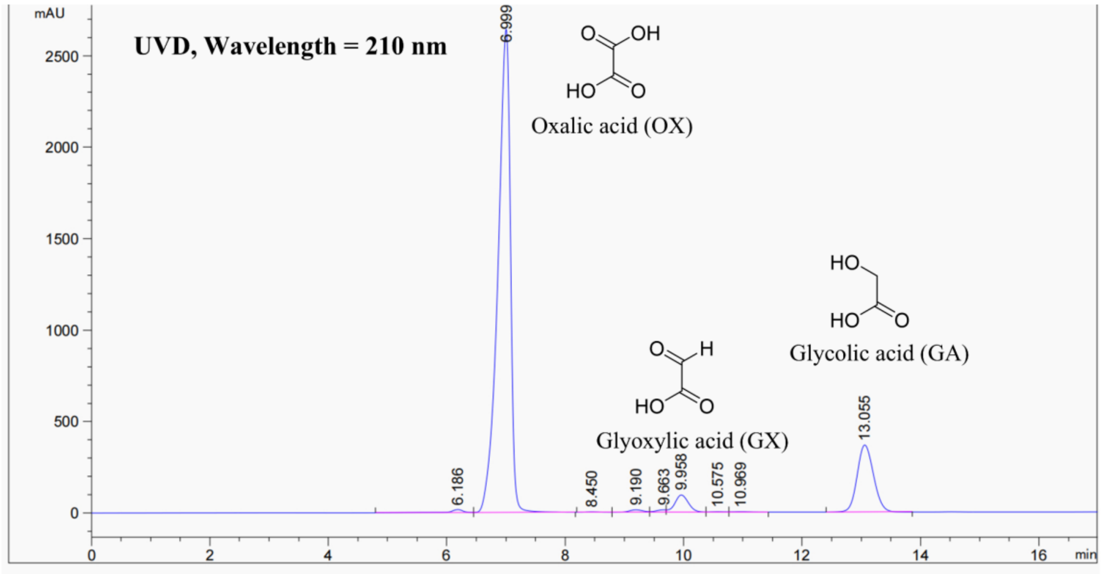

Fig. S5. HPLC spectra of the reactant and products for ECH of 100 mM OX under 10 mA cm^{-2} for 9 h.

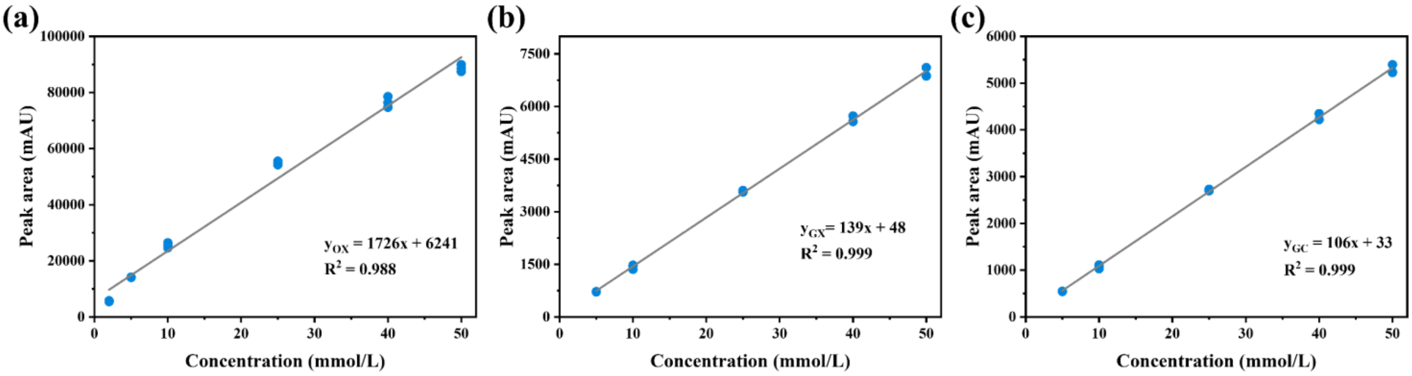

Fig. S6. The HPLC standard curves for (a) OX, (b) GX and (c) GA.

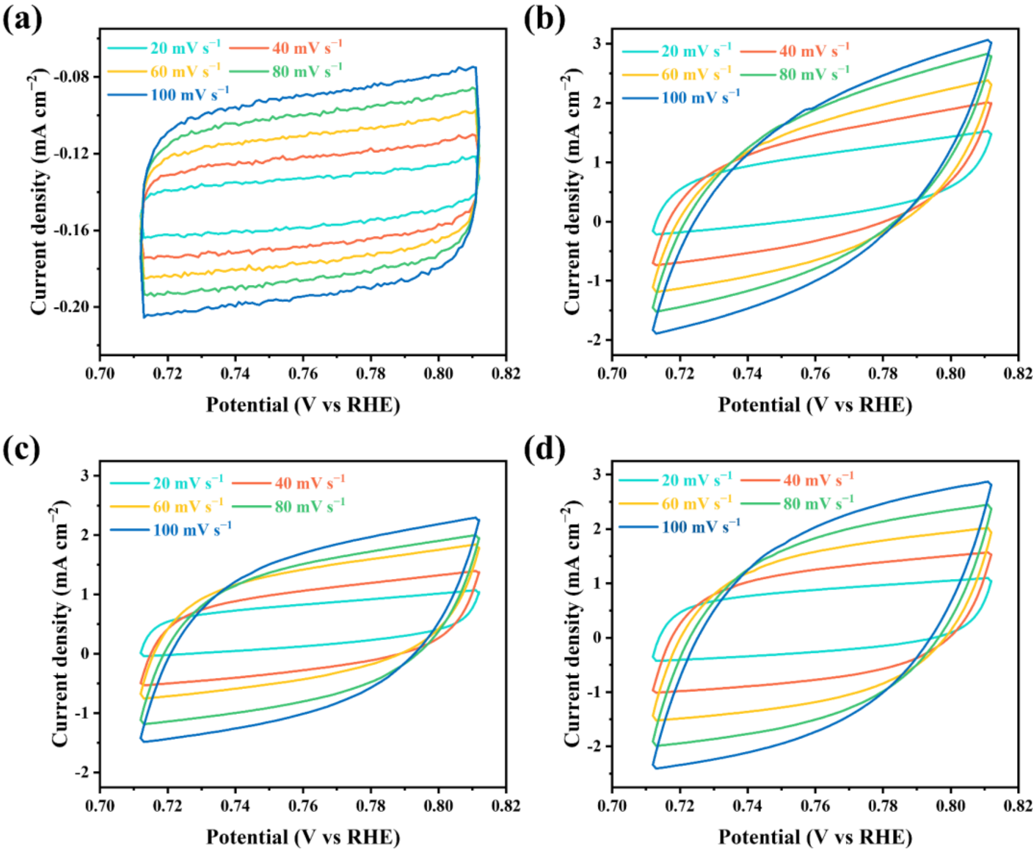

Fig. S7. CV curves of (a) Pure CC, (b) 500 ℃, (c) 600 ℃ and (d) 700 ℃ measured in non-Faradaic region (0.712 ~ 0.812 V vs RHE) of the voltammogram at different scan rates of 20, 40, 60, 80 and 100 mV s^{-1} in 0.05 M H_2SO_4 with 100 mM OX added.

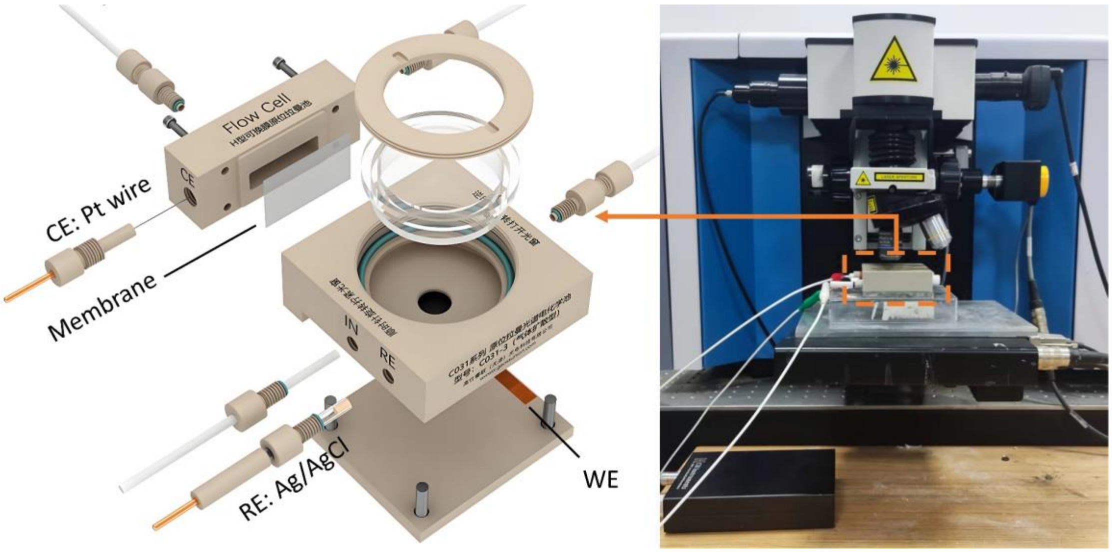

Fig. S8. The photographs of the electrolysis cell used in the *in-situ* Raman measurements.

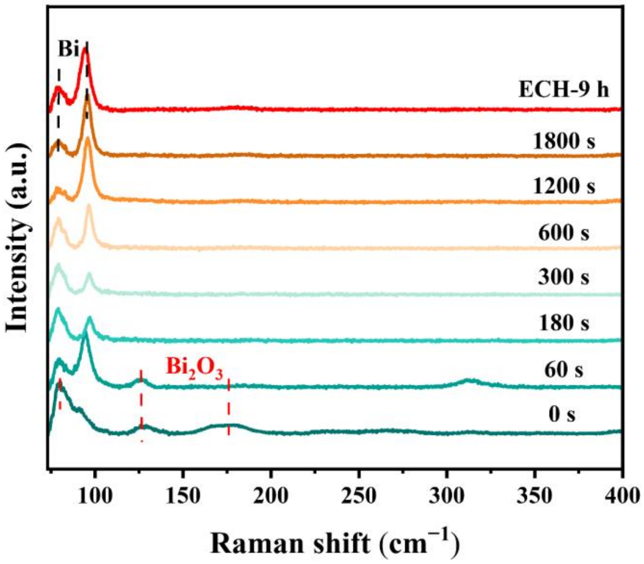

Fig. S9. Time-dependent Raman spectra of OX on Bi_2O_3@CC-700 in 0.05 M H_2SO_4 with 100 mM OX at −0.5 V vs RHE (The red curve is the Raman spectrum after ECH for 9h at the same condition.).

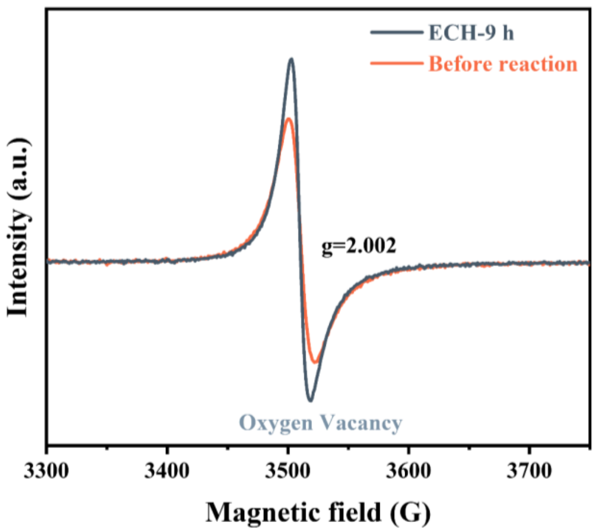

Fig. S10. EPR spectra of Bi_2O_3@CC-700 before and after ECH for 9 h.

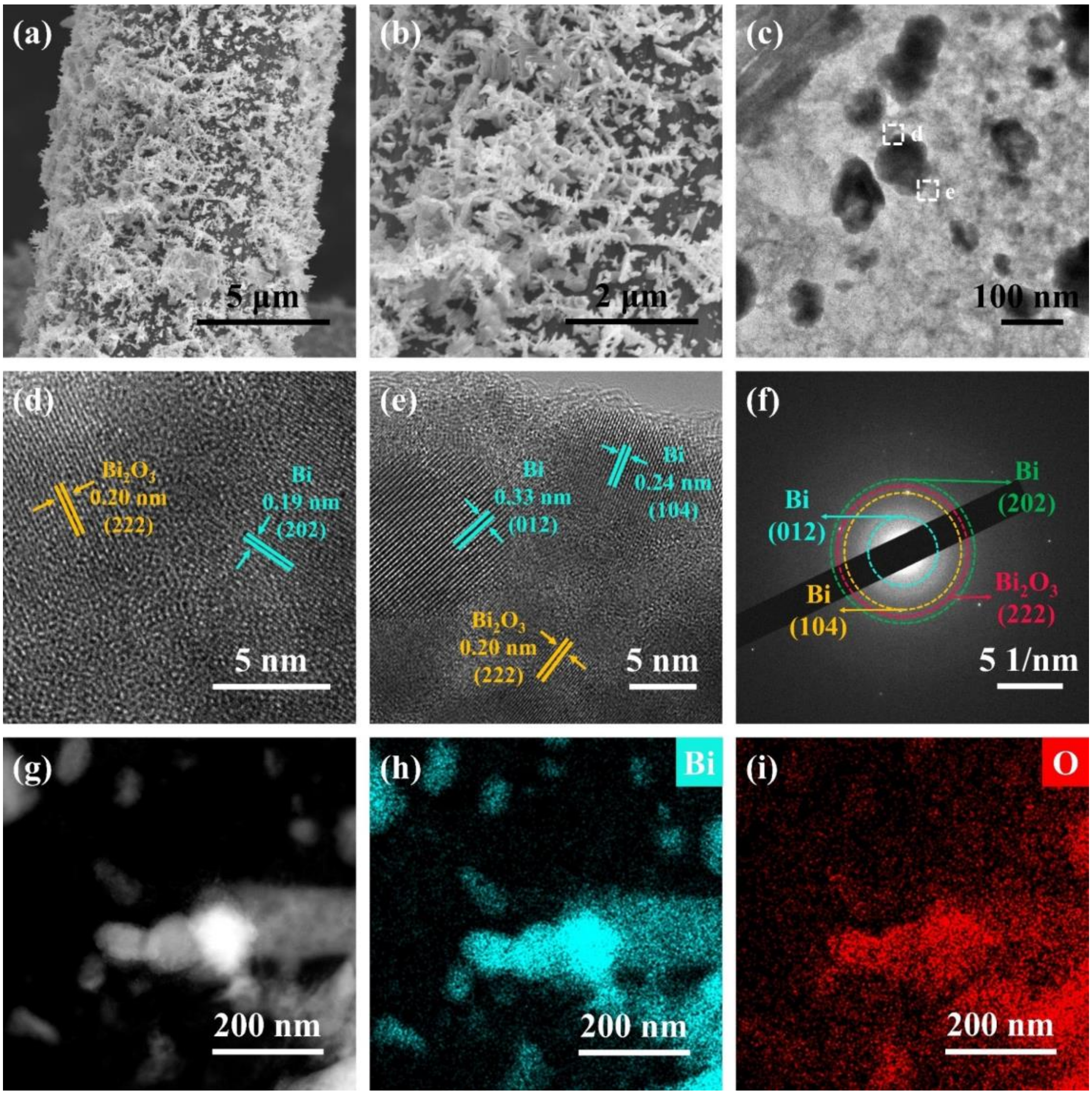

Fig. S11. (a, b) SEM images of Bi_2O_3@CC-700 after ECH for 9 h. (c) TEM image. (d, e) HRTEM images and (f) SAED pattern of Bi_2O_3@CC-700 after ECH for 9 h. (g-i) The corresponding elemental mappings.

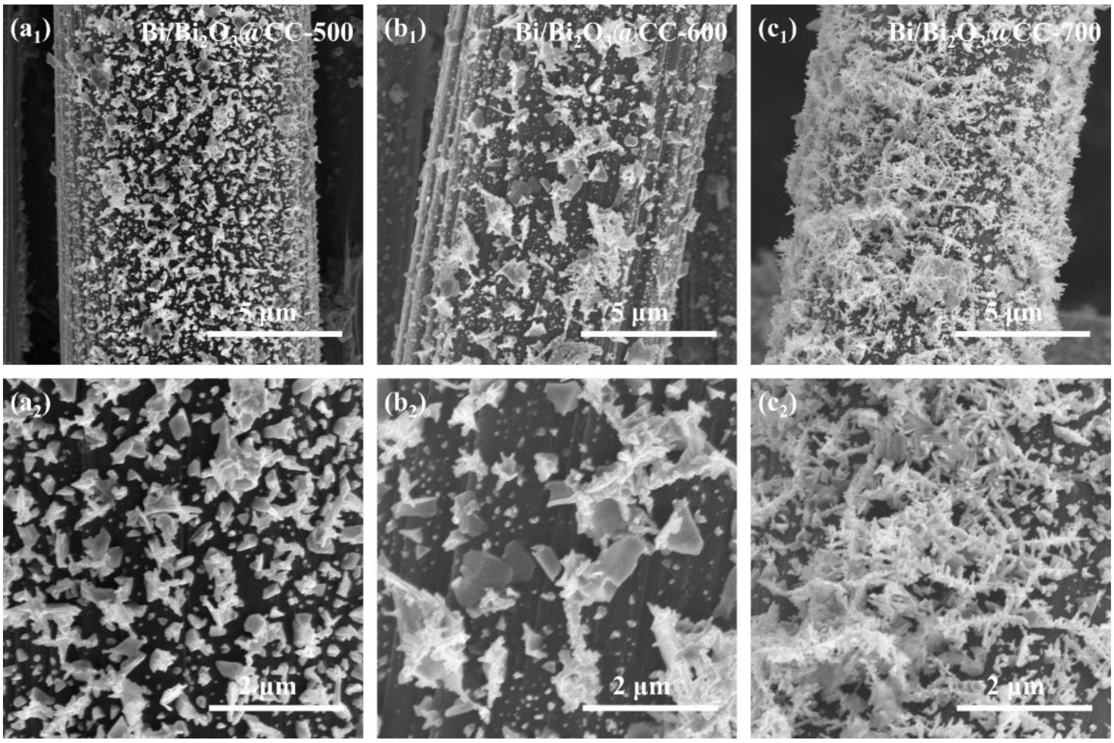

Fig. S12. The SEM images of Bi_2O_3@CC synthesized at various thermal treatment temperatures after ECH for 9 h: (a) 500 °C, (b) 600 °C, and (c) 700 °C.

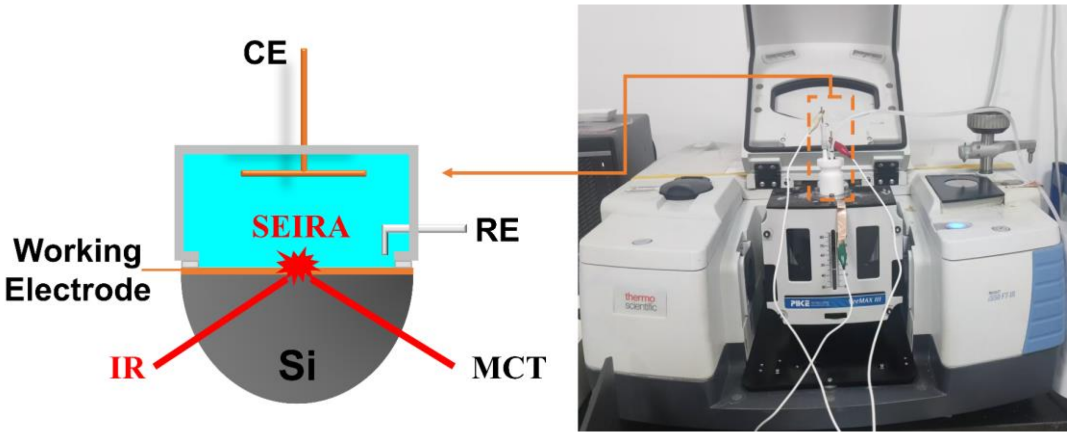

Fig. S13. The photographs of the electrolysis cell used in the *in-situ* ATR-SEIRAS measurements.

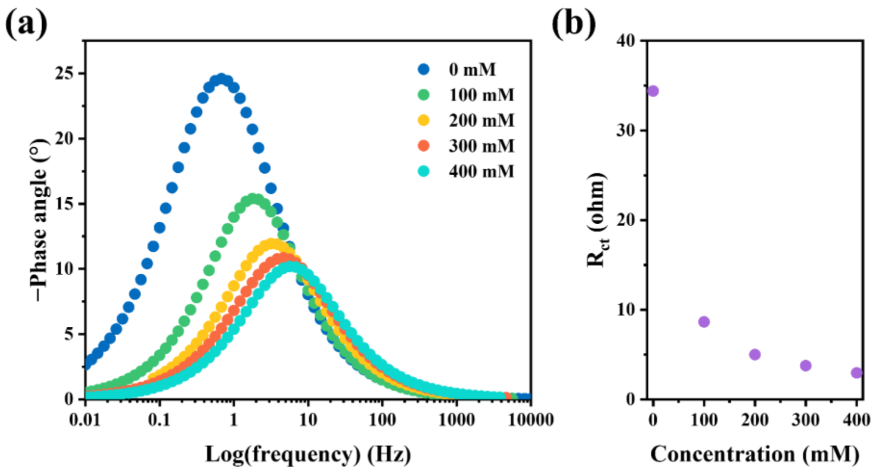

Fig. S14. (a) Bode plots of increasing gradient concentration of OX at −0.5 V vs RHE over Bi_2O_3@CC-700. (b) The corresponding correlation between the interface reaction charge transfer process resistance (R_{ct}) and the concentration of OX.

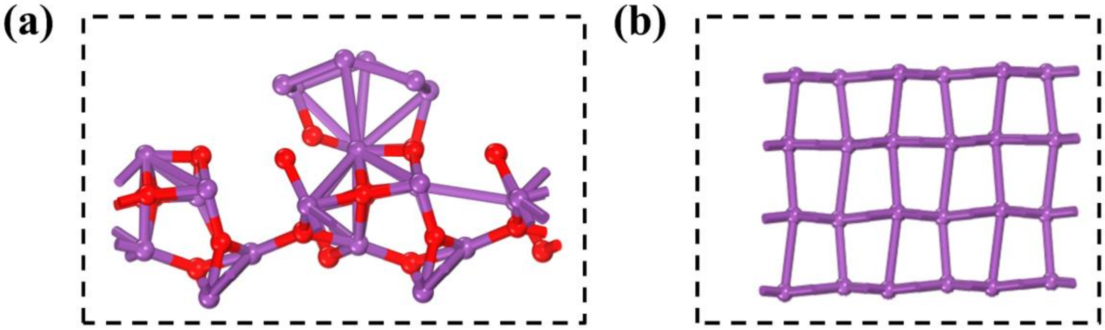

Fig. S15. The theoretical models of (a) Bi/Bi_2O_3 and (b) Bi.

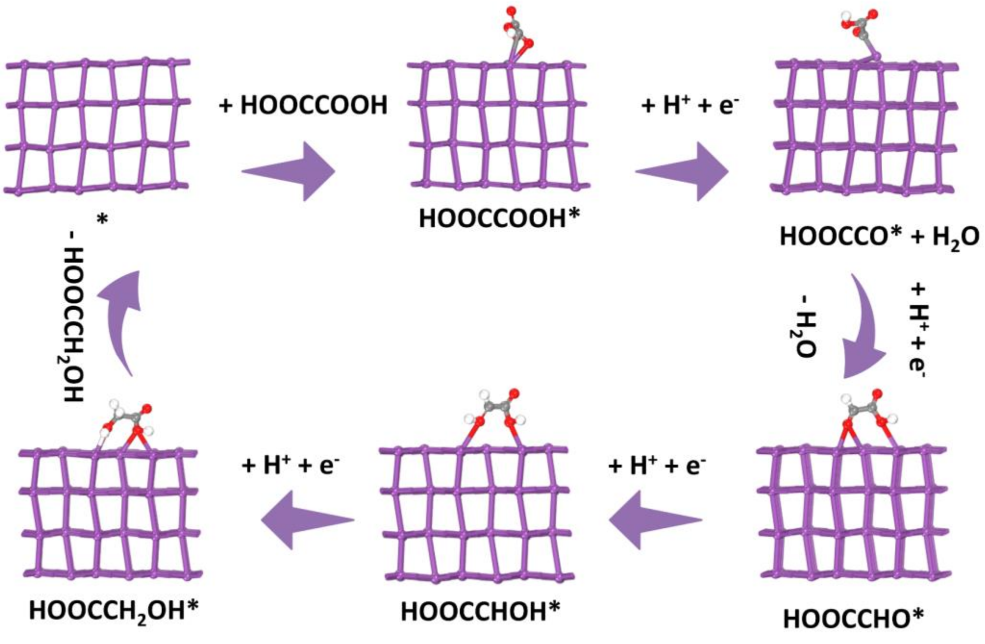

Fig. S16. Schematic illustrations of the reaction processes of OX on Bi.

Table S1. Summary of ECH of OX on different electrocatalysts.

Catalyst	Temperature (℃)	Electrolyte	Applied potential (V vs RHE)	OX Conversion (%)	GA Selectivity (%)	Faradaic efficiency (%)	Ref.
Bi_2O_3@CC-700	25	0.05 M H_2SO_4 + 100 mM OX	−0.5	82	87	61	This work
TiO_2/Ti-M	60	0.03 M OX	2 (Cell voltage)	—	50	—	5
MWNT/PyPBI/TiO_2	60	0.2 M Na_2SO_4 + 30 mM OX	2.4 (Cell voltage)	51.2	38.7	—	6
$Ti_{1-x}Zr_xO_2$	50	0.2 M Na_2SO_4 + 30 mM OX	−0.7	40.8	—	80	7
g-C_3N_4/TiO_2-NTF	R.T.	0.2 M Na_2SO_4 + 30 mM OX	−1.3 (vs Ag/AgCl)	—	76	88	8
TiNT60-E	R.T.	0.2 M Na_2SO_4 + 30 mM OX	−0.8	48	78	86	9
$GaSnO_x$/C	80	1 M OX	−0.8	~30	—	91.7	10
M-TiO_2 spheres	R.T.	100 mM OX	−0.5	—	—	73.9	11
TiO_2	50	200 mM OX	−0.74	—	70	64	12
TNT-90	60	0.2 M Na_2SO_4 + 30 mM OX	−1.0 (vs Ag/AgCl)	—	91	67	13
TiNT-HS	25	0.2 M Na_2SO_4 + 30 mM OX	−1.1 (vs Ag/AgCl)	30	—	60.8	14

Abbreviations: OX, oxalic acid; GA, glycolic acid; R.T., room temperature.

Table S2. Bi contents of various catalysts determined by ICP-OES.

Catalyst	Bi content (mg cm^{-2})
Bi_2O_3@CC-500	2.43
Bi_2O_3@CC-600	2.34
Bi_2O_3@CC-700	1.89
Bi/Bi_2O_3@CC-700	1.42
Bi_2O_3@CC-800	0.008

Table S3. The ECH performance under different reaction conditions [a].

NO.	Catalyst	Reaction Temperature (℃)	Current density (mA cm^{-2})	Applied potential (V vs RHE)	Reaction time (h)	OX Conversion (%)	GA Selectivity (%)	GX Selectivity (%)	FE (%)
1	Pure CC	25	10	—	9	38.05	56.52	29.39	24.50
2	Bi_2O_3@CC -500	25	10	—	9	72.04	67.32	17.55	56.48
3	Bi_2O_3@CC - 600	25	10	—	9	96.26	55.45	20.40	50.19
4	Bi_2O_3@CC - 700	25	10	—	9	96.70	62.82	20.18	55.73
5	Bi_2O_3@CC - 700	25	40/3	—	9	97.75	59.80	21.98	40.89
6	Bi_2O_3@CC - 700	25	50/3	—	9	96.58	85.79	4.88	40.79
7	Bi_2O_3@CC - 700	25	60/3	—	9	99.87	70.23	11.11	30.21

8	Bi_2O_3@CC - 700	25	—	−0.45	—	28.24	82.24	18.76	31.12
9	Bi_2O_3@CC - 700	25	—	−0.50	—	82.49	86.56	13.64	61.17
10	Bi_2O_3@CC - 700	25	—	−0.55	—	85.67	74.77	19.49	57.49
11	Bi_2O_3@CC - 700	25	—	−0.60	—	84.60	53.41	42.13	50.03
12	Bi_2O_3@CC - 700	25	—	−0.65	—	90.06	51.11	42.30	50.41
13	Bi_2O_3@CC - 700	25	—	−0.70	—	94.71	52.87	40.08	54.84
14	Bi_2O_3@CC - 700	35	10	—	9	89.36	81.57	12.33	62.26
15	Bi_2O_3@CC - 700	45	10	—	9	79.97	89.97	6.64	59.25
16	Bi_2O_3@CC - 700	55	10	—	9	72.84	88.93	3.55	63.15

Reaction conditions: catholyte: [a] 0.05 M H_2SO_4 with 100 mM OX; anolyte: 0.05 M H_2SO_4.

Table S4. Electrochemical properties of Pure CC, Bi_2O_3@CC-500, Bi_2O_3@CC-600, and Bi_2O_3@CC-700.

Catalyst	Overpotential at 20 mA cm^{-2} (mV)	Tafel slope (mV dec^{-1})	C_{dl} (mF cm^{-2})	R_{ct} (Ω)
Pure CC	669	393	0.5	490.8
Bi_2O_3@CC-500	519	251	11.7	20.06
Bi_2O_3@CC-600	525	206	12.4	19.29
Bi_2O_3@CC-700	507	156	16.3	11.09

Table S5. Charge transfer resistances of Bi_2O_3@CC-700 in Fig. S13.

OX Concentration (mM)	R_{ct} (Ω)
0	34.4
100	8.646
200	4.997
300	3.756
400	2.956

References

1 P. Deng, F. Yang, Z. Wang, S. Chen, Y. Zhou, S. Zaman and B. Y. Xia, *Angew Chem Int Ed Engl*, 2020, **59**, 10807-10813.

2 P. E. Blöchl, *Physical Review B*, 1994, **50**, 17953-17979.

3 R. Dronskowski and P. E. Bloechl, *The Journal of Physical Chemistry*, 1993, **97**, 8617-8624.

4 A.-P. F. Peterson A A, Studt F, Rossmeisl J, Nørskov J K, *Energy Environ. Sci.*, 2010, **3**, 1311-1315.

5 M. Sadakiyo, S. Hata, X. Cui and M. Yamauchi, *Sci Rep*, 2017, **7**, 17032.

6 J. Yang, J. Cheng, J. Tao, M. Higashi, M. Yamauchi and N. Nakashima, *ACS Applied Nano Materials*, 2019, **2**, 6360-6367.

7 M. Yamauchi, S. Hata, H. Eguchi, S. Kitano, T. Fukushima, M. Higashi, M. Sadakiyo and K. Kato, *Catalysis Science & Technology*, 2019, **9**, 6561-6565.

8 F. D. Luca, R. Passalacqua, F. P. Abramo, Siglinda, Perathoner, G. Centi and S. Abate, *Chemical Engineering Transactions*, 2021, **84**, 37-42.

9 F. P. Abramo, F. De Luca, A. Chiodoni, G. Centi, G. Giorgianni, C. Italiano, S. Perathoner and S. Abate, *Journal of Catalysis*, 2024, **429**, 115277-115285.

10 Y. Cheng, W. Xu, J. Hou and P. Kang, *ACS Catalysis*, 2023, **13**, 3676-3683.

11 W. Xu, Y. Cheng, J. Hou and P. Kang, *ChemCatChem*, 2023, **15**, e202201687.

12 L. Hao, Q. Ren, J. Yang, L. Luo, Y. Ren, X. Guo, H. Zhou, M. Xu, X. Kong, Z. Li and M. Shao, *ACS Appl Mater Interfaces*, 2023, **15**, 13176-13185.

13 S. Im, S. Saad and Y. Park, *Electrochemistry Communications*, 2022, **135**, 107204.

14 F. P. Abramo, F. De Luca, R. Passalacqua, G. Centi, G. Giorgianni, S. Perathoner and S. Abate, *Journal of Energy Chemistry*, 2022, **68**, 669-678.